Omnidirectional Wireless Power Transfer Based on Constant Coupling Polarity Concept

Zixuan Yi, *Member, IEEE*, Chenchen Li, *Student Member, IEEE*, Xue-Xia Yang, *Senior Member, IEEE*, and Meiling Li, *Member, IEEE*

***Abstract*—With the rapid development of industrial and service robots, the cross-joint dynamic wireless power transfer (WPT) technology has attracted more and more attention. Unfortunately, the current range of motion angles that can achieve WPT coverage is limited, with the maximum coverage spanning from an axial angle θ ranging from 0° to 75° and a circumferential angle φ of 360°. Currently, the realization of an omnidirectional WPT (omni-WPT) system remains elusive. This article pioneers in highlighting that maintaining constant coupling polarity (CCP) between the transmitting (*Tx*) and receiving (*Rx*) coils throughout the entire relative motion range is a fundamental requirement for achieving omni-WPT. Leveraging this insight, the cross-joint WPT with an omnidirectional operating angle is achieved for the first time. Subsequently, guidelines for designing a coupler based on CCP are provided, balancing the need for high transfer efficiency and low coupling fluctuation. To validate the effectiveness, a 13.56 MHz cross-joint omni-WPT system with $\theta \in [0°, 180°]$, $\varphi \in [0°, 360°]$ is designed, constructed and tested. The experimental results show that high efficiencies of more than 90% are achieved with low efficiency fluctuation of 1.73%. Meanwhile the output power fluctuation on the load is only 4.89%.**

***Index Terms*—Dynamic loads, dynamic wireless power transfer (WPT), magnetic resonance, omnidirectional WPT (Omni-WPT), robotic joint, robustness.**

I. Introduction

In RECENT years, dynamic loads on robotic arms have been widely found in industrial applications. More and more attention has been paid to the safe, efficient and stable power supply of these dynamic loads [1], [2], [3], [4]. At present, slip rings and brushes are the main power supplying devices used for dynamic loads [5]. However, due to the friction generated during operating, these devices are prone to metal debris and lead to accidents [6], [7]. Furthermore, the adhesion between brushes and dynamic loads at low speeds will result in resistance changes and parasitic torques that compromise the stability of the system [8]. As a result, these devices need to be replaced frequently, which leads to a significant cost increase [7].

To solve these problems, wireless power transfer (WPT) has been suggested as the most feasible strategy [2], which utilizes the magnetic or electric fields [9], [10], [11], [12]. WPT power supply eliminates the friction effect and improves the system's reliability and longevity. However, during operating, the significant variation of coupling between the transmitting (*Tx*) and receiving (*Rx*) sides results in a dramatic fluctuation of transfer efficiency and output power, which is the main obstacle of applications.

Robust circuits have been suggested to solve this issue. The operation principle is to compress the input impedance change range, in which the input impedance is seeing from the source to its load, and the change is caused by coupling fluctuations. One common method is to add one or more impendence matching networks (IMN) to the original systems [13], [14], [15], [16], such as the series *LC* circuit [17], T-type circuit [18], Π-type [19], and tunable IMNs [19], [20], [21]. Other robust circuits without using IMN have also been proposed to against coupling fluctuation. Liu et al. [22] proposed a reactance compression design to compress the variation of reflected reactance. Aldhaher et al. [23] proposed adding ac inductors in *Tx*. These robust circuits can only mitigate the effects caused by coupling fluctuations in some degree. In particular, when the coupling coefficient changes from positive to negative, this way is noneffective. Moreover, the complexity of the circuit is increased and the reliability of the system is reduced.

Robust couplers are another method to reduce the variation of coupling coefficient. This method has simple structure so the WPT system is efficient. Couplers for dynamic WPT with single-degree-of-freedom (single-DOF) are suggested [2], [3], [4], [5], [6], [7], [24], [25], in which the circumferential angle φ is take from [0°, 360°] with the axial angle θ being fixed at 0°, as shown in Fig. 1(a). These couplers can only supply power across rotating axes. In recent years, multi-DOF WPT systems that allow for simultaneous rotation of circumferential angle φ and axial angle θ, as shown in Fig. 1(b), are proposed in [10] and [11]. In [10], a magnetically coupled multi-DOF WPT system achieving rotation of $\varphi \in [0°, 360°]$ and $\theta \in [0°, 75°]$ was obtained with an ac-ac efficiency of 81% at 585 kHz. A capacitive WPT system was also proposed in [11], which realized an ac–ac efficiency of 80% at 6.78 MHz during rotation of $\varphi \in [0°, 360°]$

Manuscript received 3 April 2024; revised 25 June 2024; accepted 29 July 2024. Date of publication 8 August 2024; date of current version 7 October 2024. This work was supported in part by the National Natural Science Foundation of China under Grant 52207214 and Grant 62171270 and in part by the Natural Science Foundation of Shanghai under Grant 21ZR1423700. Recommended for publication by Associate Editor K. Park. *(Corresponding author: Meiling Li.)*

The authors are with the School of Communication and Information Engineering, Key laboratory of Specialty Fiber Optics and Optical Access Networks, Joint International Research Laboratory of Specialty Fiber Optics and Advanced Communication, Shanghai Institute for Advanced Communication and Data Science, Shanghai University, Shanghai 200444, China (e-mail: yizixuan@shu.edu.cn; 21721254@shu.edu.cn; yang.xx@shu.edu.cn; meilingli@shu.edu.cn).

Color versions of one or more figures in this article are available at https://doi.org/10.1109/TPEL.2024.3439342.

Digital Object Identifier 10.1109/TPEL.2024.3439342

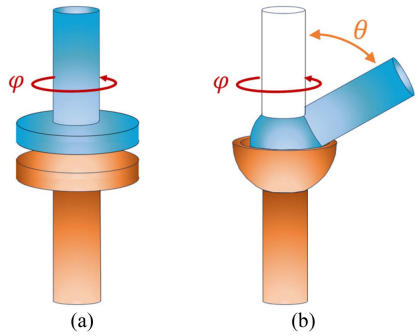

Fig. 1. (a) One degree (φ) of freedom rotation. (b) Multidegree (θ and φ) of freedom rotation.

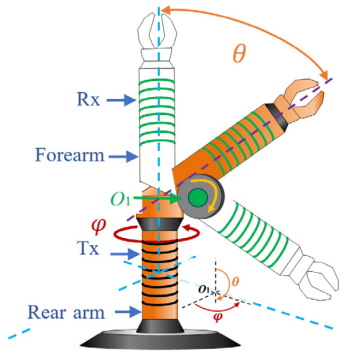

Fig. 2. Conceptual diagram of robotic arm.

and $\theta \in [0°, 26°]$. It can be found that the supply power ability in the axial angle of these designed structures is limited.

In order to achieve omnidirectional operating with $\varphi \in [0°, 360°]$ and $\theta \in [0°, 180°]$, this article proposes a highly robust omnidirectional coupler (omni-coupler) based on the concept of keeping constant coupling polarity (CCP). Through analyzing the spatial characteristics of the magnetic field generated by the coil, the coupling structure with CCP is determined. The relationship between the coupling fluctuation deviation (CFD) and the coupler design, including parameters of *Tx* and *Rx* coils and their relative motion trajectories, is studied in detail. Finally, the coupler is determined by the tradeoff between the high transfer efficiency and low coupling fluctuation.

The rest of this article is organized as follows. In Section II, the CFD is introduced to quantify the stability of the coupling coefficient in the full operating angle. In Section III, after giving the design guideline, the optimal coupler with omnidirectional WPT (omni-WPT) is designed for a practical robotic arm operating at the industrial, scientific, and medical (ISM) band. In order to prove the validity of the proposed omni-WPT, a prototype is fabricated and tested in Section IV. Finally, Section V concludes this article.

II. Analysis of the Omni-Coupler

A. Necessity of Constant Coupling Polarity (CCP) for Omni-WPT

Here, the coupling polarity is introduced first and then the discussion on why the CCP is necessary for achieving omni-WPT is made.

In the WPT system, the voltage on the *Tx* coil is

$$U_{Tx} = j\omega L_{Tx} I_{Tx} \tag{1}$$

where ω is the angular frequency of the work, L_{Tx} is the self-inductance of the transmitting coil, and I_{Tx} is the current of the transmitting coil.

The output voltage of the receiving coil is

$$U_{Rx} = j\omega M I_1 = j\omega K \sqrt{L_{Tx} L_{Rx}} I_{Tx} \tag{2}$$

where $M = K\sqrt{L_{Tx} L_{Rx}}$ is the mutual inductance between the transmitting and receiving coils, K is the coupling coefficient between the transmitting and receiving coils, and L_{Rx} is the self-inductance of the receiving coil. By solving (1) and (2), we obtain

$$K = \frac{U_{Rx}}{U_{Tx}} \sqrt{\frac{L_{Tx}}{L_{Rx}}}. \tag{3}$$

Therefore, when the voltage U_{Rx} on the *Rx* coil is in phase with the voltage U_{Tx} on the *Tx* coil, the coupling coefficient $K > 0$, indicating a positive polarity. Conversely, if they are in antiphase phase, the coupling coefficient $K < 0$, indicating a negative polarity. The meaning of CCP is that the coupling coefficient between the transceiver coils is always positive ($K > 0$) or always negative ($K < 0$) during relative omnidirectional rotation.

Any reversal of the coupling polarity of the transceiver coils during relative omnidirectional rotation would lead to the impossibility of realization of an omni-WPT system. If the coupling polarity changes during rotation, based on the continuity of the coupling coefficient function, it would indicate that at a specific position, the coupling coefficient is zero. According to (2), the output voltage U_{Rx} of the *Rx* coil would be 0 at this time, which would create a transmission blind spot and effectively prevent the achievement of omni-WPT.

B. Proposed Coupler and Main Parameters Effecting Coupling Coefficient

The omni-WPT coupler for robotic arm is presented and main parameters effecting coupling coefficient are analyzed for achieving the robust coupler. A typical robotic arm is shown in Fig. 2, which consists of a forearm and a rear ram, with the rotation point O_1. The covering angle between the axis of forearm and the axis of rear arm is $[\theta, \varphi]$. The omnidirectional motion means the circumferential rotation angle $\varphi \in [0, 360°]$ and axial rotation angle $\theta \in [0, 180°]$.

The proposed coupler that can obtain omni-WPT is shown in Fig. 3. Note that the end of the *Rx* coil, indicated by a black dot, is specified as its positive direction. The magnetic field produced by *Tx* coil is also shown in Fig. 3. It can be seen that the flux generated by *Tx* coil always flow in the positive direction of Rx coil when θ changes from 0° to 180°, which means that the coupling polarity of proposed coupler will keep constant, i.e., CCP is achieved. This feature provides a prerequisite for realizing robust omni-coupler. In practice, *Tx* and *Rx* coils could

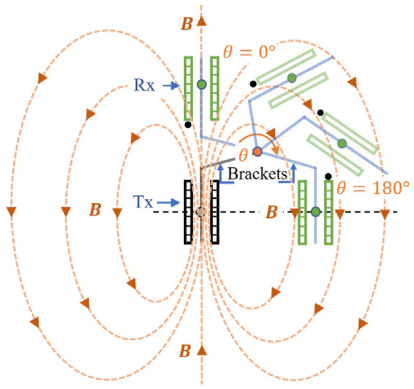

Fig. 3. Magnetic field analysis of omni-coupler at $\varphi = 0°$ and $\theta \in [0°, 180°]$.

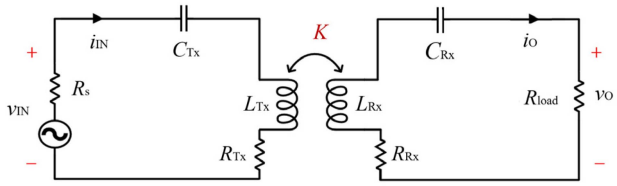

Fig. 4. Equivalent circuit of omni-WPT system.

be wrapped around the rear arm and forearm respectively, as shown in Fig. 2. Due to the circumferential rotational symmetry of the magnetic field produced by *Tx* coil, only one fixed circumferential rotation angle $\varphi = 0°$ is analyzed hereinafter.

The equivalent circuit of the proposed omni-WPT system is depicted in Fig. 4. L_m, R_m , and C_m (*m* represents *Tx* or *Rx*) are the self-inductance, coil loss and series capacitors of *Tx* and *Rx* coils, respectively. Here, C_m is used in *Tx* and *Rx* coils to form a resonant tank at operating frequency *f*. V_{in} is the ac source with internal resistance R_{s}. R_{load} is the equivalent resistance of the WPT system's load. *M* is the mutual inductance between *Tx* and *Rx* coils. The coupling coefficient between *Tx* and *Rx* coils *K* is determined as

$$K = \frac{M}{\sqrt{L_{Tx} L_{Rx}}}. \tag{4}$$

The robust WPT would be achieved when the coupling coefficient *K* is stable [7], [26], [27].

A Cartesian coordinate system (*XOY*) is established to find out the parameters effecting the coupling coefficient *K*, as shown in Fig. 5, in which the origin *O* is located at the center of *Tx* coil and the *Y*-axis is placed along the *Tx* coil's axis. Here, P_1 and P_2 are the centers of the *Rx* coil when θ is 0° and 180°, respectively. The trajectory of the center of *Rx* coil rotating around *Tx* coil is shown as the red dotted line. The structural parameters are given in Table I. In the *XOY* plane, the trajectory can be described by a semicircle with a diameter of line segment P_1P_2 and the origin of O_1. Here, the position of O_1 can be expressed as $((2r+d+D_1)/2, (L+D_2)/2)$. And the line segment O_1P_1 is radius of the trajectory (namely *R*), which can be expressed as

$$(2R)^2 = (2r + d + D_1)^2 + (L + D_2)^2. \tag{5}$$

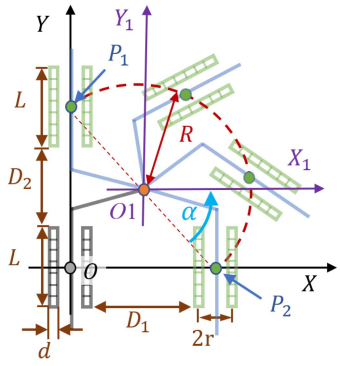

Fig. 5. Schematic diagram of $\varphi = 0°$ and $\theta \in [0, 180°]$.

TABLE I
DEFINITION OF STRUCTURAL DESIGN PARAMETERS

Parameters	Definition
D_1	Spacing between *Rx* and *Tx* coils under $\theta = 180°$
D_2	Spacing between *Rx* and *Tx* coils under $\theta = 0°$
L	Length of Tx and *Rx* solenoids
r	Radius of Tx and *Rx* solenoids
d	Wire diameter
R	Trajectory radius

Factors that affect L_m are radius *r*, length *L*, wire diameter *d* and number of turns *N* of the coil. In addition, the *M* and the L_m are both proportional to N^2 [28], which means that turns *N* does not affect *K*.

According to (4), the parameters effecting *K* are the same as to the parameters effecting the mutual inductance *M* and L_m. Therefore, the parameters that affect the coupling coefficient *K* can be summarized as

$$\{D_1, D_2, L, r, d\}.$$

C. Analysis of Coupling Fluctuation Deviation (CFD)

In order to facilitate the calculation of the coupling coefficient *K*, the parametric equation expressed in the *XOY* plane is deduced by coordinate system transformation. A coordinate system $X_1O_1Y_1$ plane is established on the rotation point O_1, whose coordinate axes are parallel to the axes of *XOY* plane as shown in Fig. 5. In the $X_1O_1Y_1$ plane, the parametric equation describing the position and the direction of *Rx* coil during rotation can be expressed as

$$\begin{cases} X_1 = R\cos(\pi - \theta)\cos\alpha + R\sin(\pi - \theta)\sin\alpha \\ Y_1 = R\sin(\pi - \theta)\cos\alpha - R\cos(\pi - \theta)\sin\alpha \end{cases} \tag{6}$$

where the angle $\alpha \in (090°)$ is between the vector $\overrightarrow{O_1P_2}$ and X_1 axis, which can be expressed as

$$\tan\alpha = \frac{L + D_2}{2r + d + D_1}. \tag{7}$$

Therefore, the equation of trajectory in the *XOY* plane be expressed through translating the $X_1O_1Y_1$ plane as follows:

$$\begin{cases} X = X_1 + \frac{2r+2d+D_1}{2} \\ Y = Y_1 + \frac{L+D_2}{2} \end{cases} \tag{8}$$

where $(2r+d+D_1)/2$ and $(L+D_2)/2$ are the translations values of horizontal and vertical coordinates, respectively.

Bring (5)–(7) into (8), the parametric equation of the trajectory in the *XOY* plane can be rewritten as (9) shown at the bottom of the this page.

The CFD is defined to quantify the stability of the coupling coefficient in the full rotating zones

$$\text{CFD} = \frac{K_{\max} - K_{\min}}{2K_{\text{ave}}} \times 100\%. \tag{10}$$

Here, $K_{\max}$, $K_{\min}$, and K_{ave} represent the maximum, minimum and numerical average of coupling coefficient during operation, respectively. The coupler has robust performance when the values of CFD are smaller. The parametric trajectory (9) could be used to analyze the impacts of parameters on CFD [28].

In order to ensure the universality of the results, all dimensions are normalized to the coil radius *r*, i.e., D_1^{nor}, D_2^{nor}, L^{nor}, r^{nor}, and d^{nor}, respectively. The calculation formula for mutual inductance *M* and self-inductance L_m is expressed as follows:

$$\begin{aligned} &M(\theta, D_1^{\text{nor}}, D_2^{\text{nor}}, L^{\text{nor}}, r^{\text{nor}}, d^{\text{nor}}) = N_1 N_2 M' \\ &= \frac{N_1 N_2 \sum_{g=-b_1}^{b_1} \sum_{h=-b_2}^{b_2} \sum_{l=-b_3}^{b_3} \sum_{c=-b_4}^{b_4} M_0(\theta, D_1^{\text{nor}}, D_2^{\text{nor}}, L^{\text{nor}}, r^{\text{nor}}, d^{\text{nor}}, g, h, l, c)}{(2b_1+1)(2b_2+1)(2b_3+1)(2b_4+1)} \end{aligned} \tag{11}$$

where

$$\begin{aligned} &M_0(\theta, x_1, x_2) \\ &= \frac{\mu_0 \sqrt{p(h, r^{\text{nor}}, d^{\text{nor}}) s(l, r^{\text{nor}}, d^{\text{nor}})}}{\pi} \\ &\int_0^{\pi} \frac{\left[\cos(\theta) - \cos(\phi) \frac{y(\delta, c, x_2)}{s(l, r, d)}\right] \Phi(\theta, x_1, x_2)}{\sqrt{v(\theta, l, c, x_2)^3}} d\phi. \end{aligned}$$

Here, *M'* is the average mutual inductance per turn; N_1 and N_2 are the number of turns of transmitting coil and receiving coil, respectively. μ_0 represents the permeability of vacuum. L_{m} can be obtained by taking *Tx* and *Rx* coils to coincide in (11).

Calculating from (9)–(11), Fig. 6 shows CFD versus normalized D_1^{nor}, D_2^{nor}, L^{nor}, with different d^{nor}. The minimum CFD obtained is about 47% within operating angle from 0° to 180°. Compared the minimum CFD is about 31% within operating angle from 0° to 75° reported in [10], this article significantly improves the operating angle (about 140%) with little sacrifice of robustness. It can be seen that the CFD is relatively stable near its minimum value. Here, the zone in which the CFD being less than 50% are defined as the available zone, which is marked as black in the Fig. 6. Meanwhile, it is seen that the available zones are observed when $L^{\text{nor}} \geq 2.5$, which is independent of d^{nor}.

III. Design of the Optimal Omni-coupler

As discussed above, the minimum CFD can be obtained by different parameter groups, which means that the choice is not unique for the respective of CFD. Therefore, the transfer efficiency is taken into consideration to obtained the optimal coupler, which would be determined by finding the most efficient point in the available zone. In this section, after discussing the coupling fluctuation and transfer efficiency, the design guideline is presented.

A. Losses of the Coils

The coil-to-coil efficiency η_c is discussed in detail in [29] and [30]. The maximum system efficiency (η_m) can be estimated using (12) as described in [29], [30], and [31]

$$\eta_m = 1 - \frac{2}{k\sqrt{Q_1 Q_2}} \tag{12}$$

where the quality factors Q_i ($i = 1, 2$) of *Tx* and *Rx* coils can be given as

$$Q_i = \frac{\omega L_i}{R_i} \tag{13}$$

where $\omega = 2\pi f$, L_i is self-inductance and R_i is the loss resistance of *Tx* and *Rx* coils, respectively. *Tx* and *Rx* coils are identical in this article, which means $R_1 = R_2 = R_{\text{loss}}$.

The loss of the coils R_{loss} is primarily caused by two factors: ohmic resistance R_{ohm} and far-field radio resistance R_r

$$R_{\text{loss}} = R_{\text{ohm}} + R_r. \tag{14}$$

Butterworth has conducted a series of studies to determine the alternating current (ac) resistance of solenoids [32]. When operating at very high frequency, that is, the ratio of the wire diameter to the skin penetration depth $\rho = d/\tau$ is greater than 10, the ohmic resistance of a solenoid can be calculated using

$$R_{\text{ohm}} = R_l \left(\gamma_1 + \frac{1}{2}\frac{d}{s}(\gamma_2\mu_1 + \gamma_3\mu_2)\right). \tag{15}$$

Here, d is the wire diameter, s is the distance of successive wires. Functions γ_1, γ_2, and γ_3 are dependent on d/s, while μ_1 and μ_2 vary with $L/2r$. The ac resistance of uncoiled wire R_l can be derived by solving the power loss equation [18], as demonstrated

$$\int_0^{\frac{2\pi}{\omega}} i^2 R_l dt = \int_0^{\frac{2\pi}{\omega}} \int_0^{l_w} \frac{i^2}{\pi\tau\sigma d} dx dt \tag{16}$$

$$\begin{cases} X = \frac{\sqrt{(2r+d+D_1)^2+(L+D_2)^2}}{2}\left(\cos(\pi-\theta)\cos\arctan\frac{L+D_2}{2r+d+D_1} + \sin(\pi-\theta)\sin\arctan\frac{L+D_2}{2r+d+D_1}\right) + \frac{2r+d+D_1}{2} \\ Y = \frac{\sqrt{(2r+d+D_1)^2+(L+D_2)^2}}{2}\left(\sin(\pi-\theta)\cos\arctan\frac{L+D_2}{2r+d+D_1} - \cos(\pi-\theta)\sin\arctan\frac{L+D_2}{2r+d+D_1}\right) + \frac{L+D_2}{2} \end{cases} \tag{9}$$

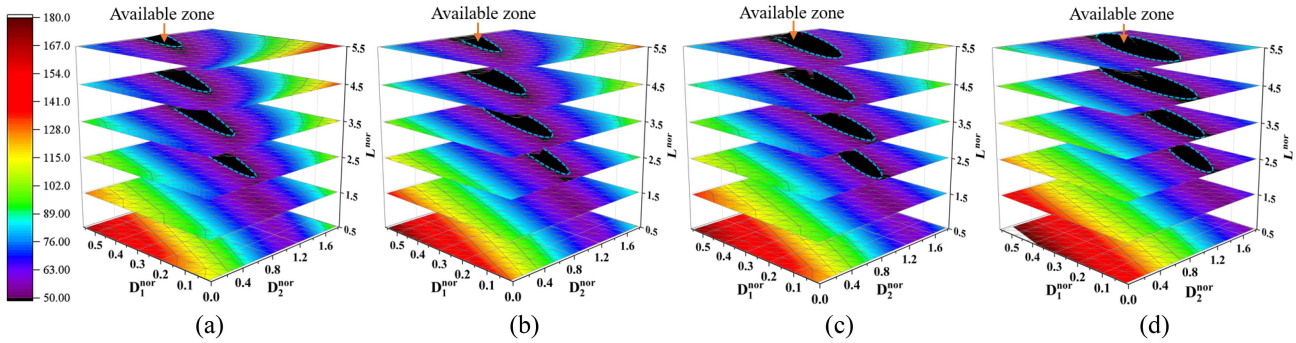

Fig. 6. CFD versus normalized parameters D_1^{nor}, D_2^{nor}, L^{nor} through numerical calculation (9)–(11). (a) $d^{\text{nor}} = 0.05$. (b) $d^{\text{nor}} = 0.1$. (c) $d^{\text{nor}} = 0.2$. (d) $d^{\text{nor}} = 0.3$.

where l_w, τ, σ, and d are the total length, the skin penetration, conductivity and wire diameter, respectively. And τ is defined as

$$\tau = \sqrt{\frac{2}{\omega\mu\sigma}}. \tag{17}$$

In which μ is permeability and is often taken as $4\pi \times 10^7$. The solution of (16) is

$$R_l = \frac{l_w\sqrt{f\mu}}{d\sqrt{\pi\sigma}}. \tag{18}$$

The radio resistance R_r can be obtained by the well-known formula [33]

$$R_r = 320\pi\left(N\frac{\pi(2r)^2}{4\lambda^2}\right)^2. \tag{19}$$

Here, λ is the operating wavelength.

B. Transfer Efficiency

According to (12) and (13), the η_m can be expressed as

$$\eta_m = 1 - \frac{2R_{\text{loss}}}{\omega M}. \tag{20}$$

Thus, at a certain operating frequency f, the η_m is determined by M and R_{loss}. And an increase of turn N leads in an increase of M and R_{loss}. In this article, two identical solenoids are employed as *Tx* and *Rx* coils, i.e., $N_1 = N_2$. According to (11), the M can be expressed as

$$\begin{aligned} M &= N_1N_2 \times M' \\ &= N^2 \times M' \\ &\propto N^2 \end{aligned} \tag{21}$$

where M' is the average mutual inductance per turn; N_1 and N_2 are the number of turns of transmitting coil and receiving coil, respectively.

To determine the optimal value of η_m, M and R_{loss} are normalized by N^2 to obtain M_0 and R_0. Consequently, (20) can be rephrased as follows:

$$\eta_m = 1 - \frac{2}{\omega}\frac{R_{\text{loss}}/N^2}{M/N^2} = 1 - \frac{2}{\omega}\frac{R_0}{M_0}. \tag{22}$$

Therefore, the η_m is positive correlation to M_0/R_0.

The transfer efficiency from *Tx* coils to *Rx* one is closely related by their losses, which are further affected by the operating frequency f and the coil radius r. Therefore, the practical operating frequency f and radius of coils r must be determined at first. This is what is often done in practical applications. Due to the typical diameter of a robotic arm is about 80 mm, $r = 40$ mm is selected as the design example in this article. The operating frequency f is chosen as 13.56 MHz, which is within the ISM band from ITU radiocommunication sector.

By solving (11), (14)–(19) and (22), the values of η_m at the maximum M_0/R_0 are presented in Fig. 7, which describes the impact of $D_1^{\text{nor}}, D_2^{\text{nor}}$, L^{nor} on efficiency. It is worthy to note that the value of N is chosen to maximize M_0/R_0, which means that the N is same and optimized for the fixed d^{nor} and L^{nor}. It can be seen from Fig. 7 that the results of two cases are unavailable. The first case is $\{d^{\text{nor}}, L^{\text{nor}}\} = \{0.2, 0.5\}$ or $\{0.3, 0.5\}$. In this case, wire diameter d^{nor} is too large while the length of the solenoid L^{nor} is too short to form a solenoid. The second case is $d^{\text{nor}} = 0.05$ and $L^{\text{nor}} \geq 1.5$, or $d^{\text{nor}} = 0.1$ and $L^{\text{nor}} \geq 3.5$, or $d^{\text{nor}} = 0.2$ and $L^{\text{nor}} \geq 4.5$. In this case, the wire diameter d^{nor} is too small and the length of solenoid L^{nor} is too long, which results in the wavelength effects. That means the inconsistent current direction along the solenoids appears would lead to a sharp deterioration of mutual inductance [29], [34]. It can be concluded from Fig. 7 that the η_{m} becomes smaller as D_1^{nor} or D_2^{nor} increases, and remains almost constant with varying d^{nor} and L^{nor}.

C. Design Guideline of Optimal Omni-coupler

Since normalized parameters are discussed rather than specific parameters in Sections II-C and III-B, the results of the CFD are universal while the efficiency is determined by the radius of solenoid r and the operating frequency f. As mentioned above, $r = 40$ mm and $f = 13.56$ MHz are selected in this article. The design guideline of optimal omni-coupler is summarized as follow.

First, determining d^{nor}. According to aforementioned analysis, the values of minimum CFD and efficiency change slightly as the d^{nor} changes. However, the amount of space occupied by wires and fabricating cost will increase with the increasing of d^{nor}. Therefore, a smaller value of d^{nor} is preferable. But, a small

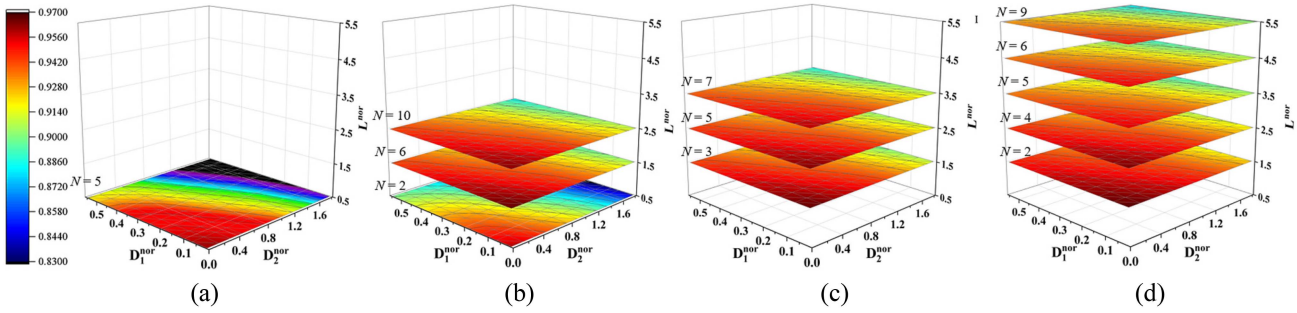

Fig. 7. η_m versus variables D_1^{nor}, D_2^{nor}, L^{nor} through solving (11), (14)–(19) and (22). (a) $d^{\text{nor}} = 0.05$. (b) $d^{\text{nor}} = 0.1$. (c) $d^{\text{nor}} = 0.2$. (d) $d^{\text{nor}} = 0.3$.

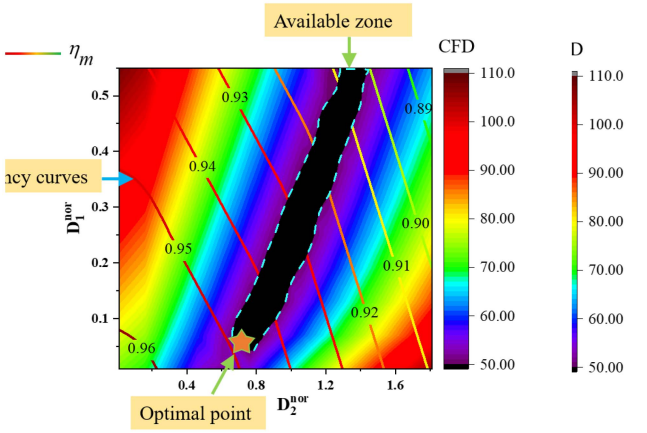

Fig. 8. Contour map of CFD and η_{m} at $d^{\text{nor}} = 0.1$ and $L^{\text{nor}} = 2.5$. ★: The optimal point.

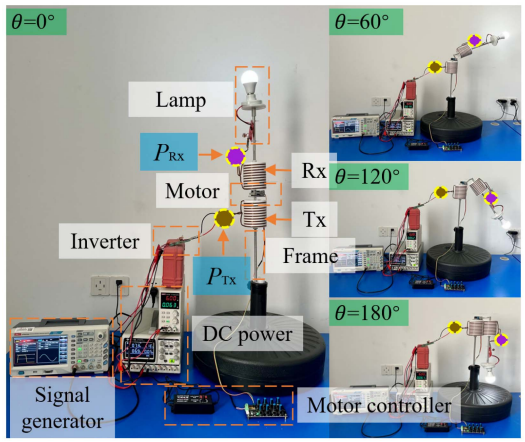

Fig. 9. Omni-WPT system under different rotating degrees ($\theta = 0°$, 60°, 120°, and 180°).

TABLE II
PARAMETERS OF OPTIMAL COUPLER

D_1	2.8 mm	D_2	30.4 mm
L	100 mm	r	40 mm
d	4 mm	N	10

d^{nor} will result in a long wire, which will lead to the wavelength effect. Thus, $d^{\text{nor}} = 0.1$ is selected here.

Second, determining L^{nor} and N. When $d^{\text{nor}} = 0.1$, on the one hand, the available zone appears only if $L^{\text{nor}} \geq 2.5$, as shown in Fig. 6(b); on the other hand, the efficient transfer can be achieved only if $L^{\text{nor}} \leq 2.5$, as shown in Fig. 7(b). Therefore, in order to possess simultaneously low CFD and high transfer efficiency, $L^{\text{nor}} = 2.5$ is selected here. Here, N is equal to 10.

Finally, determining D_1^{nor}andD_2^{nor}. The contour map of over-printing CFD and η_{m} at $d^{\text{nor}} = 0.1$, $L^{\text{nor}} = 2.5$ is shown in Fig. 8. The available zone and isoefficiency curves are shown in Fig. 8. Through determining the most efficient point in the available zone, the optimal parameters are found to be $D_1^{\text{nor}} = 0.07$ and $D_2^{\text{nor}} = 0.76$, which is marked by a pentagram in Fig. 9.

According to the above analysis, the parameters of optimal coupler for this design case ($r = 40$ mm and $f = 13.56$ MHz) can be determined as given in Table II.

IV. Fabrication and Measurement

Based on the omni-coupler obtained in Section III-C, an omni-WPT system for robotic arm, whose equivalent circuit is shown in Fig. 4, is constructed and measured. The configuration of the prototype is firstly introduced. Then, the transfer efficiency and output power of the prototype are measured and analyzed.

A. Configuration of the Prototype

Based on the practical parameters as shown in Table II, an omni-coupler is fabricated and a WPT system for robotic arm is constructed as shown in Fig. 9. The *Tx* side includes an inverter and a *Tx* coil. The *Rx* side consists of an *Rx* coil and a lamp as the load. Normally, the robot arms used in factories are made of plastic housing with metal frames for guaranteeing the mechanical strength. Here, two metal frames being made of aluminum alloy with a diameter of 10 mm are comprised in the prototype. Since the metal frames are parallel to the magnetic flux produced by coils, the magnetic field distribution of the coupler is almost not change, which will be verified by following experimental results. The housing of the robotic arms is made of Poly tetra fluoroethylene and serves as the support for the *Tx* and *Rx* coils. Two motors are used to provide the driving force for the forearm (*Rx* coil) rotating along the axial angle θ and the circumferential angle φ, respectively.

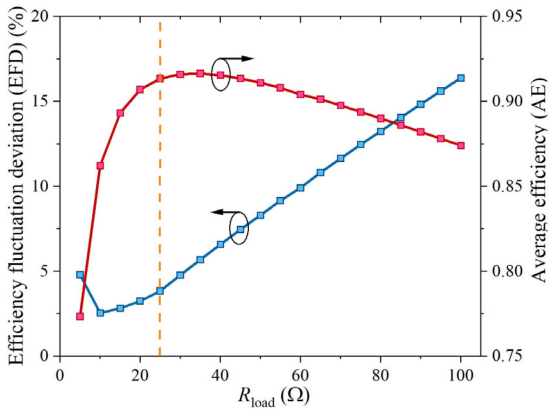

Fig. 10. Efficiency fluctuation deviation (EFD) and average efficiency (AE) of omni-coupler with respect to the different R_{load}.

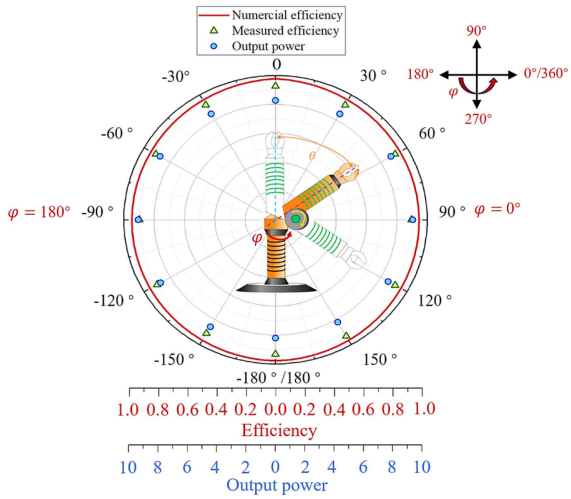

Fig. 11. Transfer efficiency and output power versus axial rotation angle θ. The values of $\theta \in [0°, 180°]$ and $\theta \in [0°, -180°]$ are obtained at $\varphi = 0°$ and $\varphi = 180°$, respectively.

Measured by a vector network analyzer (VNA, Keysight N5247A), the R_{loss} of the fabricated *Tx* and *Rx* coils are 1.59 Ω and 1.55 Ω, respectively, the self-inductance L_m ($m = Tx$ and *Rx*) of the *Tx* and *Rx* coils are 7.28 and 7.19 uH, respectively. According to (13), the quality factors Q of *Tx* and *Rx* coil are 390 and 395, respectively. The series capacitance C_m for resonance tank of *Tx* and *Rx* coils are 18.9 and 19.2 pF according to

$$2\pi f = \frac{1}{\sqrt{LC_m}}. \tag{23}$$

B. Experimental Verifications

The measured CFD is calculated to be 49.8% which is in good agreement with the calculation result of 46.7%. The slight deviation between calculation and measurement is mainly caused by the disturbance on the magnetic field induced by the metal frame, steering gear and the model manufacturing error.

To determine the optimal R_{load}, the efficiency fluctuation deviation (EFD) and average efficiency (AE) of the omni-coupler with different loads is measured and shown in Fig. 10. The EFD

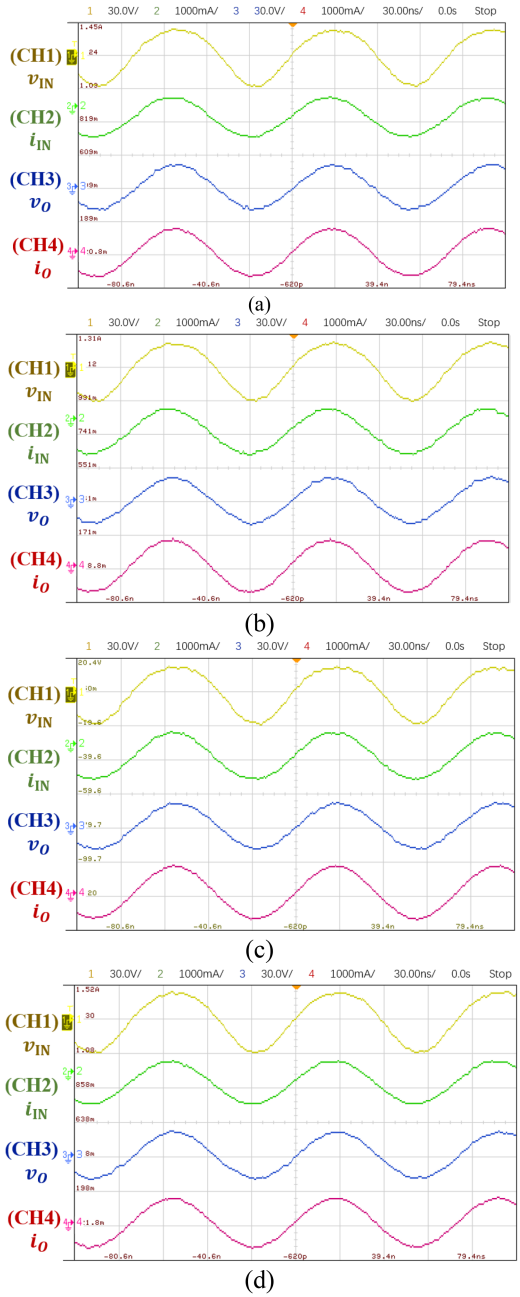

Fig. 12. Measured waveforms of the proposed omni-coupler under peak-to-peak input voltage of 55 V, operating frequency of 13.56 MHz, and $R_{\text{load}} = 25\ \Omega$ for four rotating degrees; CH1: 30 V/div, CH2: 1000 mA/div, CH3: 30 V/div and CH4: 1000 mA/div. (a) $\theta = 0°$. (b) $\theta = 60°$. (c) $\theta = 120°$. (d) $\theta = 180°$.

is defined to quantify the efficiency variation over the operating angle, which can be calculated as

$$\text{EFD} = \frac{\eta_c^{\max} - \eta_c^{\min}}{2\eta_c^{\text{ave}}} \times 100\%. \tag{24}$$

Here, $\eta_c^{\max}$, $\eta_c^{\min}$ and η_c^{ave} represent the maximum, minimum and numerical average of efficiency during operation, respectively. It can be seen from Fig. 10 that the minimum EFD is about 2.5% in which $R_{\text{load}} = 10\ \Omega$. The AE can be calculated

TABLE III
MEASURED COUPLING COEFFICIENT, VOLTAGE, CURRENT, AND POWER VALUES AT DIFFERENT ROTATIONAL ANGLES

θ (deg)	Coupling coefficient (measured)	V_{in} (V)	I_{in} (A)	P_{in} (W)	V_{out} (V)	I_{out} (A)	P_o (W)	Efficiency (%)
0	0.112	55	1.30	8.94	40.84	1.62	8.27	92.53%
30	0.064	55	1.35	9.28	41.07	1.65	8.47	91.29%
60	0.049	55	1.42	9.76	41.86	1.68	8.79	90.02%
90	0.048	55	1.46	10.04	42.54	1.70	9.04	90.01%
120	0.054	55	1.41	9.69	41.87	1.67	8.74	90.21%
150	0.071	55	1.34	9.21	41.30	1.66	8.57	93.07%
180	0.122	55	1.28	8.25	40.49	1.62	8.20	93.17%

as

$$\mathrm{AE} = (\eta_{0^\circ} + \eta_{30^\circ} + \ldots + \eta_{180^\circ})/7. \tag{25}$$

Here, η_θ ($\theta = 0^\circ$, 30° … 180°) is the measured efficiency of the omni-coupler with different axial angle θ. The maximum AE is about 91.6%, in which $R_{\mathrm{load}} = 35\ \Omega$. Based on the tradeoff between EFD and AE, the final R_{load} is selected as 25 Ω, which has both high efficiency and high robustness.

The transfer efficiency and output power of the omni-WPT system with $\varphi = 0^\circ$, θ from 0° to 180° with interval 30° and $\varphi = 180^\circ$, θ from 0° to -180° with interval 30° is shown in Fig. 11. The results are measured under operating frequency of 13.56 MHz and the output load resistance of 25 Ω. The experimental results as shown in Table III show that the transfer efficiency of the omni-coupler is more than 90% and the EFD is just only 1.73%, which is calculated by (24). Meanwhile, the output power fluctuation deviation (OPFD) under constant input voltage is only 4.89%, which can be calculated as

$$\mathrm{OPFD} = \frac{P_{\max} - P_{\min}}{2P_{\mathrm{ave}}} \times 100\%. \tag{26}$$

Here, $P_{\max}$, $P_{\min}$, and P_{ave} represent the maximum, minimum and numerical average of efficiency during operation, respectively.

In addition, it can be seen from Fig. 11 that the experimental values of the transfer efficiency and output power have nearly consistent performance when circumferential angle φ is rotated from 0° to 180°. In fact, the spatial position relationship between *Tx* and *Rx* coils is unchanged after rotating along φ, and the abovementioned consistent performance of experimental results also prove this perspective. In other words, the proposed omni-coupler can achieve simultaneously the circumferential angle $\varphi \in [0^\circ, 360^\circ]$ and axial angle $\theta \in [0^\circ, 180^\circ]$, i.e., omnidirectional operation with a constant efficiency.

Input voltage/current and output voltage/current waveforms are captured at four rotation degrees (0°, 60°, 120°, 180°) by using oscilloscope at point P_{TX} and P_{RX} in Fig. 11, which are presented in Fig. 12. The peak-to-peak input voltage is 55 V, with the operating frequency of 13.56 MHz, and R_{load} of 25 Ω. CH1 and CH2 are the input voltage and input current of the *Tx,* and CH3 and CH4 are the output voltage and output current of the *Rx*.

TABLE IV
COMPARISON WITH EXISTING WPT SYSTEMS OPERATING AT ROTATIONAL FREEDOM

	Haven and seo [9]	Zhang et al. [10]	Liang et al. [11]	Houran et al. [12]	**This article**
Frequency	13.56 MHz	585 kHz	6.78 MHz	852.5 kHz	13.56 MHz
Type	IPT	IPT	CPT	IPT	IPT
FOA	-	45%	14%	-	100%
Efficiency	60%	81%	80%	84%	90%
EFD	-	2.61%	1.85%*	2.60%*	1.73%
Power	4 W	3 W	7 W	6.5 W	8 W
OPFD	-	6.65%	4.04%*	-	4.89%

*: the results are obtained from the plot of experimental results. FOA: fractional operating angle, which the values take from 0% to 100%. EFD: efficiency fluctuation deviation calculated by (24). OPFD: output fluctuation deviation calculated by (26).

To demonstrate the advancements of the proposed omni-WPT system for robotic arm, a comparison with recently published WPT systems operating at rotational freedom are given in Table IV. The omnidirectional coupler with efficiency fluctuation 1.73% based on CCP concept has the largest operating angle (axial rotation angle $\theta \in [0, 180^\circ]$) and highest transfer efficiency (>90%). It can be seen from Table IV that the proposed omni-WPT system has significant advantages in operating angle as well as transfer efficiency.

V. CONCLUSION

This article proposes an omni-WPT system with high robust performance for robotic arm. After analyzing the influence of parameters on CFD in detail, the design guideline for achieving optimal coupler with advantages of high robustness and high efficiency is given. To prove the validity of the proposed concept, a prototype operating at 13.56 MHz is designed, constructed and tested. Without additional complex control system, the omni-WPT system realizes a stable transfer efficiency with EFD of 1.73%. The efficiency is higher than 90% during omnidirectional motion, and the OPFD under constant input voltage is only 4.89%. For large angle omnidirectional rotating power supply applications, the coupler design method provides a suitable

option. The proposed omni-WPT system could be applied at robotic arms and any other multi-DOF sceneries.

REFERENCES

[1] Q. Jiang and F. Chang, "A novel antibody population optimization based artificial immune system for rotating equipment anomaly detection," *J. Mech. Sci. Technol.*, vol. 34, pp. 3565–3574, Sep. 2020.

[2] K. Song et al., "A rotation-lightweight wireless power transfer system for solar wing driving," *IEEE Trans. Power Electron.*, vol. 34, no. 9, pp. 8816–8830, Sep. 2019.

[3] S. Luo, A. Qiao, and Q. Tang, "A magnetic coupled rotary composite force sensor," *IEEE Sensors J.*, vol. 20, no. 2, pp. 745–751, Jan. 2020.

[4] P. Procaházka, "Electromagnetic simulator of rotating machine blades for noncontact sensor dynamic testing," *IEEE Trans. Instrum. Meas.*, vol. 67, no. 6, pp. 1506–1508, Jun. 2018.

[5] L. Wang, J. Li, H. Chen, and Z. Pan, "Radial-flux rotational wireless power transfer system with rotor state identification," *IEEE Trans. Power Electron.*, vol. 37, no. 5, pp. 6206–6216, May 2022.

[6] J. P. C. Smeets, L. Encica, and E. A. Lomonova, "Comparison of winding topologies in a pot core rotating transformer," in *Proc. 12th Int. Conf. Optim. Elect. Electron. Equip.*, 2010, pp. 103–110.

[7] G. Gao and W. Chen, "Design challenges of wind turbine generators," in *Proc. IEEE Elect. Insul. Conf.*, 2009, pp. 146–152.

[8] S. Gao et al., "Novel design of multi-DOF motor position estimation based on wireless power transmission modeling," *IEEE Trans. Ind. Electron.*, vol. 71, no. 3, pp. 2853–2863, Mar. 2024.

[9] N. Ha-Van and C. Seo, "Analytical and experimental investigations of omnidirectional wireless power transfer using a cubic transmitter," *IEEE Trans. Power Electron.*, vol. 65, no. 2, pp. 1358–1366, Feb. 2018.

[10] C. Zhang, D. Lin, and S. Y. R. Hui, "Ball-joint wireless power transfer systems," *IEEE Trans. Power Electron.*, vol. 33, no. 1, pp. 65–72, Jan. 2018.

[11] H. W. R. Liang, C. K. Lee, and S. Y. R. Hui, "Design, analysis, and experimental verification of a ball-joint structure with constant coupling for capacitive wireless power transfer," *IEEE J. Emerg. Sel. Topics Power Electron.*, vol. 8, no. 4, pp. 3582–3591, Dec. 2020.

[12] M. A. Houran, X. Yang, and W. Chen, "Two-degree-of-freedom WPT system using cylindrical-joint structure for applications with movable parts," *IEEE Trans. Circuits Syst. II: Exp. Briefs*, vol. 68, no. 1, pp. 366–370, Jan. 2021.

[13] Y. Shao, H. Zhang, M. Liu, and C. Ma, "Explicit design of impedance matching networks for robust MHz WPT systems with different features," *IEEE Trans. Power Electron.*, vol. 37, no. 9, pp. 11382–11393, Sep. 2022.

[14] M. Liu, S. Liu, and C. Ma, "A high-efficiency/output power and low-noise megahertz wireless power transfer system over a wide range of mutual inductance," *IEEE Trans. Microw. Theory Techn.*, vol. 65, no. 11, pp. 4317–4325, Nov. 2017.

[15] M. Liu, C. Zhao, J. Song, and C. Ma, "Battery charging profile-based parameter design of a 6.78-MHz class E2 wireless charging system," *IEEE Trans. Ind. Electron.*, vol. 64, no. 8, pp. 6169–6178, Aug. 2017.

[16] M. Liu, J. Song, and C. Ma, "Active class E rectifier for DC output voltage regulation in megahertz wireless power transfer systems," *IEEE Trans. Ind. Electron.*, vol. 67, no. 5, pp. 3618–3628, May 2020.

[17] N. O. Sokal and A. D. Sokal, "Class E-A new class of high-efficiency tuned single-ended switching power amplifiers," *IEEE J. Solid-State Circuits*, vol. 10, no. 3, pp. 168–176, Jun. 1975.

[18] M. Liu, Y. Qiao, S. Liu, and C. Ma, "Analysis and design of a robust class E2 DC–DC converter for megahertz wireless power transfer," *IEEE Trans. Power Electron.*, vol. 32, no. 4, pp. 2835–2845, Apr. 2017.

[19] S. Liu, M. Liu, S. Yang, C. Ma, and X. Zhu, "A novel design methodology for high-efficiency current-mode and voltage-mode Class-E power amplifiers in wireless power transfer systems," *IEEE Trans. Power Electron.*, vol. 32, no. 6, pp. 4514–4523, Jun. 2017.

[20] Y. Liu and H. Feng, "Maximum efficiency tracking control method for WPT system based on dynamic coupling coefficient identification and impedance matching network," *IEEE Trans. Emerg. Sel.*, vol. 8, no. 4, pp. 3633–3643, Dec. 2020.

[21] Y. Li, W. Dong, Q. Yang, J. Zhao, L. Liu, and S. Feng, "An automatic impedance matching method based on the feedforward-backpropagation neural network for a WPT system," *IEEE Trans. Ind. Electron.*, vol. 66, no. 5, pp. 3963–3972, May 2019.

[22] K. Zhang, W. Gao, R. Shi, Z. Yan, B. Song, and A. P. Hu, "An impedance matching network tuning method for constant current output under mutual inductance and load variation of IPT system," *IEEE Trans. Power Electron.*, vol. 35, no. 10, pp. 11108–11118, Oct. 2020.

[23] S. Aldhaher, D. C. Yates, and P. D. Mitcheson, "Load-Independent class E/EF inverters and rectifiers for MHz-switching applications," *IEEE Trans. Power Electron.*, vol. 33, no. 10, pp. 8270–8287, Oct. 2018.

[24] Y. Zhang, J. Yang, D. Jiang, D. Li, and R. Qu, "Design, manufacture, and test of a rotary transformer for contactless power transfer system," *IEEE Trans. Magn.*, vol. 58, no. 2, Feb. 2022, Art. no. 8400206.

[25] A. Abdolkhani, A. P. Hu, and N.-K. C. Nair, "A double stator through-hole type contactless slipring for rotary wireless power transfer applications," *IEEE Trans. Energy Convers.*, vol. 29, no. 2, pp. 426–434, Jun. 2014.

[26] Z. Zhang, H. Pang, A. Georgiadis, and C. Cecati, "Wireless power transfer—An overview," *IEEE Trans. Ind. Electron.*, vol. 66, no. 2, pp. 1044–1058, Feb. 2019.

[27] C. Cai et al., "Design and optimization of load-independent magnetic resonant wireless charging system for electric vehicles," *IEEE Access*, vol. 6, pp. 17264–17274, 2018.

[28] S. I. Babic and C. Akyel, "Calculating mutual inductance between circular coils with inclined axes in air," *IEEE Trans. Magn.*, vol. 44, no. 7, pp. 1743–1750, Jul. 2008.

[29] Z. Yi, M. Li, B. Muneer, and Q. Zhu, "High-Efficiency mid-range inductive power transfer employing alternative-winding coils," *IEEE Trans. Power Electron.*, vol. 34, no. 7, pp. 6706–6721, Jul. 2019.

[30] Z. Yi, M. Li, B. Muneer, G. He, and X.-X. Yang, "Self-Resonant antisymmetric planar coil for compact inductive power transfer system avoiding compensation circuits," *IEEE Trans. Power Electron.*, vol. 36, no. 5, pp. 5121–5134, May 2021.

[31] E. Waffenschmidt and T. Staring, "Limitation of inductive power transfer for consumer applications," in *Proc. 13th Eur. Conf. Power Electron. Appl.*, 2009, pp. 1–10.

[32] S. Butterworth, "On the alternating current resistance of solenoidal coils," *Proc. Roy. Soc. London. Ser. A, Math. Phys. Eng. Sci.*, vol. 107, no. 744, pp. 693–715, Dec. 1925.

[33] C. A. Balanis, "Loop antennas," in *Antenna Theory: Analysis and Design*, 3rd ed. Hoboken, NJ, USA: Wiley, 2005, pp. 231–246.

[34] L. Zhu, L. Wang, M. Wu, C. Zhao, and L. Yu, "Precise modeling and design of self-resonant for high-efficiency mid-range wireless power transfer system," *IEEE Trans. Power Electron.*, vol. 38, no. 6, pp. 7848–7862, Jun. 2023.

Zixuan Yi (Member, IEEE) was born in Taiyuan, China, in 1991. He received the B.S. degree in electronic engineering and information science and the Ph.D. degree in electromagnetism field and microwave technology from the University of Science and Technology of China, Hefei, China, in 2014 and 2019, respectively.

He is currently an Associate Professor with the School of Communication and Information Engineering, Shanghai University, Shanghai, China. His research interests include wireless power transfer systems, microwave passive components, metamaterial, and antennas.

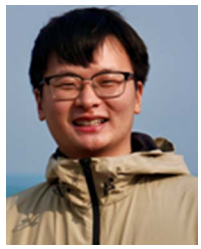

Chenchen Li (Student Member, IEEE) was born in Henan, China, in 1998. He received the B.S. degree in electronic information engineering from the School of Physics & Electronic Information Engineering, Henan Polytechnic University, Henan, China, in 2021. He is currently working toward the master of engineering degree in communication and information system with the School of Communication and Information Engineering, Shanghai University, Shanghai, China.

His research interests include wireless power transfer and ac–dc converter.

Xue-Xia Yang (Senior Member, IEEE) received the B.S. and M.S. degrees in radio physics from Lanzhou University, Lanzhou, China, in 1991 and 1994, respectively, and the Ph.D. degree in electromagnetic field and microwave technology from Shanghai University, Shanghai, China, in 2001.

From 1994 to 1998, she was a Teaching Assistant and a Lecturer with Lanzhou University. From 2001 to 2008, she was a Lecturer and an Associate Professor with Shanghai University, Shanghai, China. She is currently a Professor and the Head of the Antennas and Microwave R&D Center, Shanghai University. She has authored or coauthored over 180 technical journal and conference papers. She is also a frequent Reviewer for more than ten scientific journals. Her research interests include antennas theory and technology, computational electromagnetics and microwave power transmission.

Dr. Yang is a member of the Committee of Antenna Society of China Electronics Institute and a Senior Member of China Electronics Institute. She is an Associate Editor for *Journal of Shanghai University* (Science edition).

Meiling Li (Member, IEEE) was born in Wuhu, China, in 1988. She received the B.S. degree in electronic information engineering from Anhui University, Hefei, China, in 2010, and the Ph.D. degree in electromagnetism field and microwave technology from the University of Science and Technology of China, Hefei, China, in 2016.

She was a Postdoctoral Researcher with the Department of Electronic Engineering and Information Science, University of Science and Technology of China, Hefei, China. She is currently an Associate Professor with the School of Communication and Information Engineering, Shanghai University, Shanghai, China. Her research interests include wireless power transfer systems, frequency selected surfaces, absorbing materials and structures, and microwave circuits.